

# Modeling drifter trajectories and ensemble dispersion from the Ocean Training Course 2025

Samantha Kucher

Vadim Bertrand

## Table of contents

<b>1</b>	<b>Introduction</b>	<b>2</b>
<b>2</b>	<b>Instruments, data and methods</b>	<b>2</b>
2.1	Drifters deployed during the campaign . . . . .	3
2.1.1	MELODI . . . . .	3
2.1.2	SPOT . . . . .	5
2.2	Satellite and drifter data . . . . .	6
2.2.1	Satellite-derived gridded products . . . . .	6
2.2.2	Drifter data . . . . .	7
2.3	Modeling of drifter trajectories . . . . .	8
2.3.1	Linear combination . . . . .	9
2.3.2	Maxey-Riley framework . . . . .	10
2.3.3	Model evaluation . . . . .	12
2.4	Pair dispersion . . . . .	12
<b>3</b>	<b>Results</b>	<b>12</b>
3.1	Modeling of drifter trajectories . . . . .	13
3.1.1	Linear combination . . . . .	13
3.1.2	Maxey-Riley framework . . . . .	15
3.2	Pair dispersion . . . . .	15
<b>4</b>	<b>Discussion</b>	<b>20</b>
4.1	Modeling of drifter trajectories . . . . .	20
4.1.1	Linear combination . . . . .	20
4.1.2	Maxey-Riley framework . . . . .	21
4.2	Pair dispersion . . . . .	21
<b>5</b>	<b>Conclusion</b>	<b>22</b>
<b>6</b>	<b>Acknowledgements</b>	<b>23</b>

# 1 Introduction

Better understanding of particle transport in the ocean is crucial to reduce marine plastic pollution. The life of microplastics in the ocean is nonetheless complex: they can be transported through long distances by currents and gyres, mixed in turbulent flows, broken into smaller pieces, and sinked by biofouling ([Sutherland et al., 2023](#)). Recent laboratory experiments and theoretical developments have been made to study the influence of particle size, shape and density ([Clark et al., 2020](#)), ([DiBenedetto et al., 2022](#)), ([R. Calvert et al., 2024](#)). There is a growing interest in narrowing the gap between controlled experiments and real-world conditions found in the ocean.

Oceanic models are able to forecast the ocean state several days ahead, but they are not capable of resolving the small scales corresponding to particle transport. The combined effect of waves, currents and wind must be taken into account to predict the drift of passive tracers ([Christensen et al., 2018](#)). Parametrizing the movement of particles in wavy, turbulent flows thus presents a fundamental challenge ([Van Sebille et al., 2020](#)), ([Sutherland et al., 2023](#)).

It has been shown that large non-Lagrangian floating particles experience a drift larger than the Stokes drift ([Ross Calvert et al., 2021](#)). This is due to the object oscillation relative to the free surface and its submergence, which changes continuously with the wave slope. The size of the object with respect to the wavelength is a determining factor in the drifting velocity. In the ocean, the dynamics of currents strongly impacts the propagation of wave fields ([Quilfen & Chapron, 2019](#)), and therefore modifies the particles trajectories. The impact of wind has also been addressed, using a leeway modeling approach to gain physical understanding of the forces that play a role in the drift of floating objects ([Wagner et al., 2022](#)). This model, however, does not accurately predict the trajectories of floating particles. Such prediction is given by the Maxey-Riley set for inertial surface particles [Beron-Vera et al. \(2019\)](#).

Satellite-tracked drifters have been studied in the North Atlantic ([S. Elipot et al., 2016](#)), and an *in-situ* study has been made in the Florida Current ([Olascoaga et al., 2020](#)). In the latter, the trajectory of buoys has been followed for one week. The authors successfully modeled the experimental data using a framework derived from the Maxey-Riley equations.

This project aims to reconstruct the trajectory of drifters deployed during the expedition and to better understand how physical processes govern their motion. We thus need to take into account the satellite measurements of sea surface deformation, wave induced currents and wind speed. We employ a two folded approach: (i) in first approximation a linear combination of the surface currents, Stokes drift and direct wind-force, and (ii) the full equations describing the dynamics of floating inertial particles in the ocean: the Maxey-Riley set. These two methods will allow us to decompose and analyze the individual forces governing the drifter's motion, providing deeper insights into the underlying dynamics.

We focus here on deterministic modellings of the drift. However, given the inherent chaotic nature of the problem and the uncertainties carried by our observations of oceanic and atmospheric variables, stochastic approaches might be relevant to simulate ensemble of probable and realistic trajectories, rather than one *incorrect* estimate. One challenge is to control the dispersion of simulated ensembles to accurately cover the distribution of possible trajectories. To address this question we study the relative dispersion over time of several ensembles of drifters deployed at the same space-time position.

## 2 Instruments, data and methods

This section describes the two types of drifters deployed during OTC25, as well as the data and trajectory reconstruction methods used in our analysis. We first present the design of the MELODI and SPOT drifters. Next, we introduce the different satellite-derived and drifter datasets (including the preprocessing steps applied when relevant). Finally, we detail the Lagrangian statistics used to characterize the drift dynamics, the trajectory reconstruction methods implemented, and the metrics employed to evaluate them.

## 2.1 Drifters deployed during the campaign

Figure 1 shows a photograph of all drifter types deployed during the campaign, with the exception of the Sofar Spotter. At the time of writing, only eOdyn MELODI and IGE SPOT data are available, and we therefore focus on these two types. However, it should be noted that 16 OpenMetBuoy, 4 CLS MARGE-T II, and 1 Sofar Spotter buoy were also deployed. Including these additional drifters would strengthen our analysis, as we will discuss in Section 4.



Figure 1: Types of drifters deployed during the OTC25 campaign between Tromsø and Nice. There was also a Sofar drifter not shown in the picture. Photo taken by Joël Marc.

### 2.1.1 MELODI

The MELODI ([“MELODI,” 2024](#)) is a surface drifter developed by the company eOdyn. Although we are only interested in the drifter’s position, it also measures surface currents, surface temperature and wave parameters. The position is determined using several satellite constellations, with a sampling frequency of 1 hour. The drifter uses the Iridium satellite network to transmit its data. It is powered by four Li-ion 3500 mAh, 3.7 V batteries and a 6 W solar panel, which allows it to operate for at least several months. Thanks to its low-profile, see Figure 2, the MELODI drifter is expected to be only weakly affected by wind drift.

From Tromsø to Nice, 18 MELODI drifters were deployed in various locations: in the North Sea and its Lofoten eddy, in the North Atlantic (including during a storm event), before and after the Strait of Gibraltar (within the Alboran eddy), and in the western Mediterranean Sea. This can be seen in Figure 3.

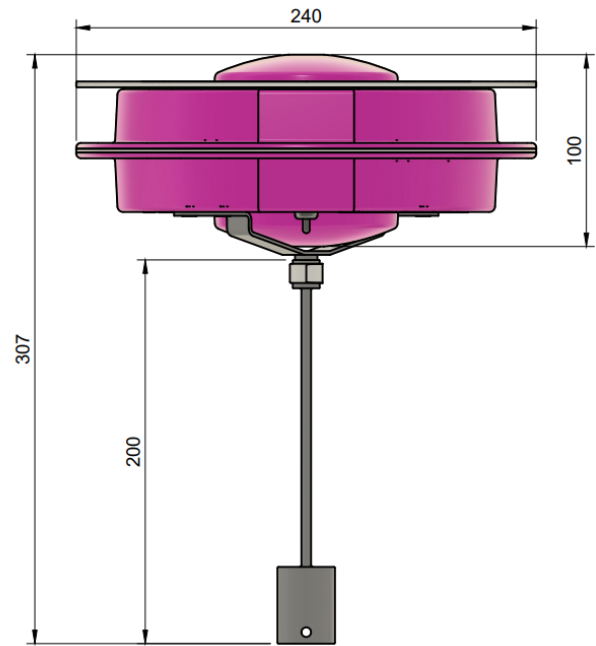


Figure 2: Design of the MELODI drifter

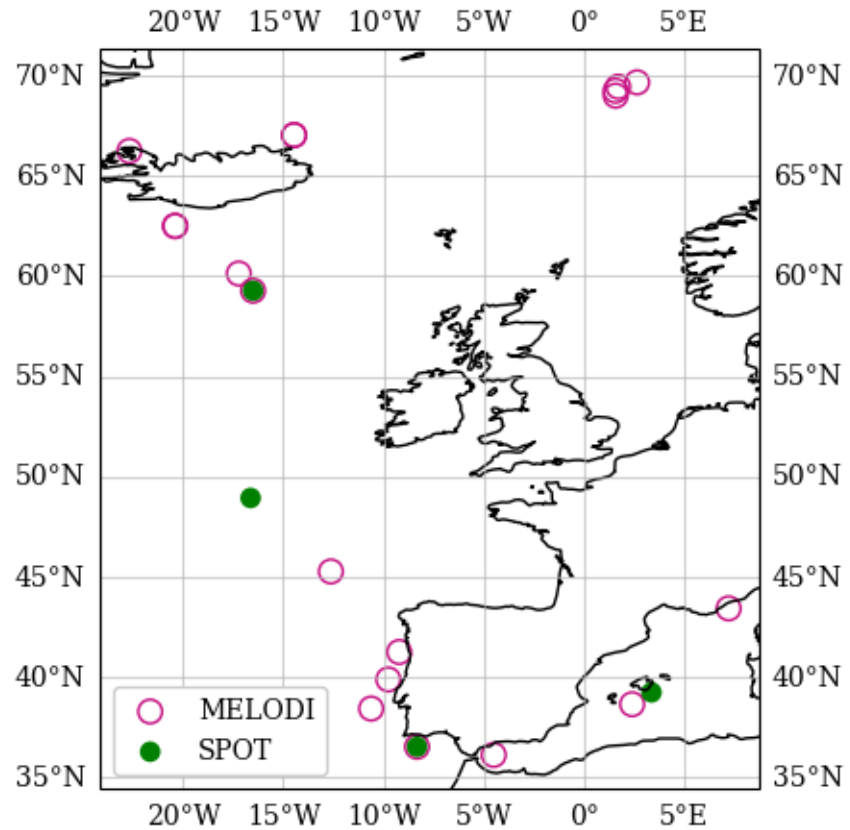


Figure 3: MELODI and SPOT drifter deployments during the OTC25 campaign.

### 2.1.2 SPOT

The SPOT (“SPOT,” 2024) is a home-made surface drifter designed and developed at Institut des Géosciences de l’Environnement (IGE). Its design is very simple, see Figure 4: a weighted waterproof jar containing a GPS tracer powered by external batteries. The GPS tracer is a SPOT Trace, which uses the Globalstar satellite network to transmit its position every 30 minutes. External batteries (4 LR20 alkaline 1.5V 13Ah) allow the drifter to operate for up to 6 months and counting at the time of writing.

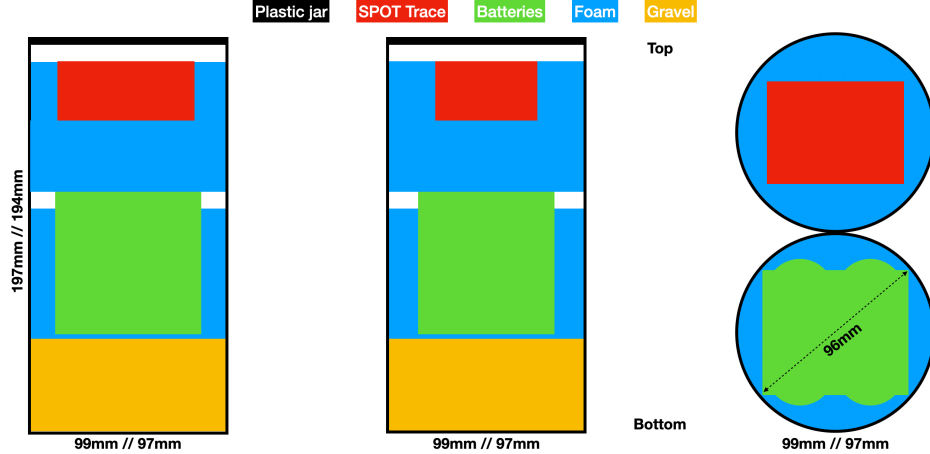


Figure 4: Design of the SPOT drifter

During the first deployments we noticed that the SPOT drifters exhibited an orbital motion around their vertical axis and we suspected that it was the cause for the observed effective sampling frequency being larger than the nominal 30 minutes (see Figure 6). To mitigate this motion we designed a dynamic anchor attached to the bottom of the drifter. Being at sea we had to reuse material available aboard the ship: old sails and steel wire ropes, as visible in Figure 5.



Figure 5: SPOT drifter with a dynamic anchor

The last five drifters deployed in the Mediterranean Sea were equipped with this anchor. Using the drifter data presented in Section 2.2.2 it seems that the anchor was effective in improving the effective sampling frequency, as shown in the left panel of Figure 6. However, the right panel of Figure 6 indicates that, among the drifters deployed in the Mediterranean Sea, drifter #19 stopped emitting very shortly after deployment for an unknown reason, while drifters #16 and #18 beached soon after deployment, leaving only drifters #17 and #20 active for more than a month. In addition, the Mediterranean Sea is known for its quieter sea state compared to the North Atlantic and the Bay of Biscay, which could explain the improved effective sampling resolution. Further analysis is therefore required to confirm whether the drogue was indeed effective.

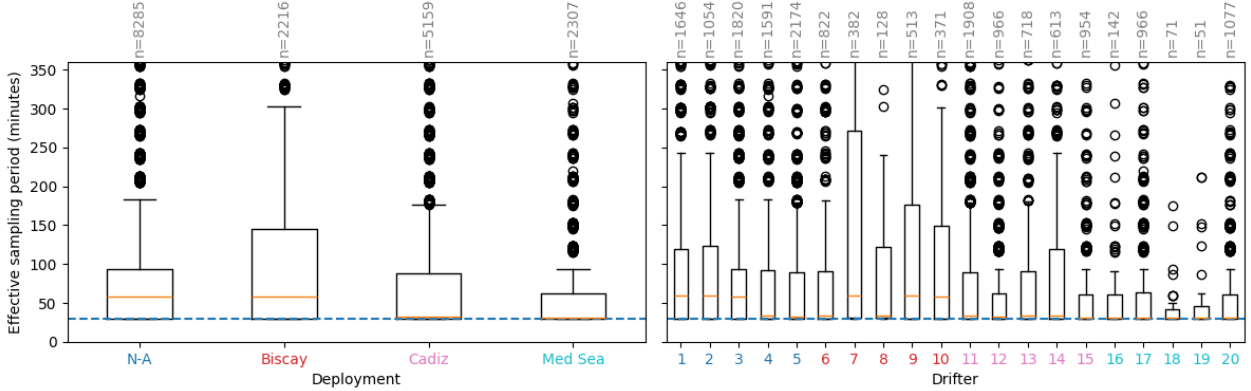


Figure 6: SPOT drifters effective sampling period. The dashed blue line indicates the nominal sampling period of 30 minutes.

## 2.2 Satellite and drifter data

Our analysis requires both maps of geophysical quantities (surface currents, waves, winds) and lagrangian drifter trajectories.

### 2.2.1 Satellite-derived gridded products

Geophysical quantities of interest are derived from satellite observations, assimilated in physical models of varying complexity.

#### 2.2.1.1 Sea Surface Height

VarDyn is a variational mapping method jointly reconstructing Sea Surface Height (SSH) and Sea Surface Temperature (SST) (Le Guillou et al., 2025). The version used in our analysis assimilates both SWOT KaRin and Nadir altimeters data and produces daily  $0.05^\circ \times 0.05^\circ$  maps. This dataset provides both SSH and sea surface currents, derived from the SSH field.

#### 2.2.1.2 Sea Surface Wind

Wind acts both directly on the drifter (the leeway) and indirectly through its effect on waves and currents. We use the wind velocity and stress at the surface from the  $0.125^\circ \times 0.125^\circ$  hourly ECMWF bias corrected product (WIND\_GLO\_PHY\_L4\_NRT\_012\_004, 2024) developed by the Royal Netherlands Meteorological Institute.

#### 2.2.1.3 Sea State

Waves also affect drifter trajectories through the Stokes drift. We employ the Stokes drift obtained by assimilating significant wave height in the wave model MFWAM, available in the  $0.083^\circ \times 0.083^\circ$  hourly Global Ocean Waves Analysis and Forecast product (GLOBAL\_ANALYSISFORECAST\_WAV\_001\_027, 2023) developed by Mercator Ocean International.

## 2.2.2 Drifter data

Starting from the raw GPS positions transmitted by the drifters, we perform several preprocessing steps before using them in our analysis.

### 2.2.2.1 L0 version

The L0 version of the data consists of datasets containing the original timestamps and positions (latitude and longitude) for each drifter, complemented by its deployment date and time. Each record also includes the time interval between successive measurements.

### 2.2.2.2 L1 version

The L1 version of the data is produced by applying the following Quality Control (QC) steps to the L0 dataset:

1. Spurious GPS locations were removed following the procedure described by Shane Eliot et al. (2016),
2. Curated trajectories were divided into segments whenever the time gap between two consecutive timestamps exceeded 6 hours,
3. Segments shorter than 1 day are discarded.

As shown in Table 1, these QC steps result in only a small reduction in the number of MELODI drifter observations. In contrast, about 20% of the SPOT observations were discarded, primarily due to transmission issues that caused large gaps in the original trajectories and consequently led to many short segments being removed.

Table 1: Number of observations and segments in L0 and L1 versions for SPOT and MELODI datasets.

Dataset	# Observations		# Segments	
	L0	L1	L0	L1
SPOT	24503	19846	20	189
MELODI	47399	46837	19	39

### 2.2.2.3 L2 version

Trajectories are resampled at a regular time interval of 1 hour using a linear interpolation for the positions and the velocities are then computed using central differences.

An example of L0, L1 and L2 trajectories for a SPOT drifter is shown in Figure 7. It can be seen that the L0 trajectory contains some spurious points, which are removed in the L1 and L2 versions. Holes in the L1 and L2 trajectories correspond to gaps larger than 6 hours in the original data. Holes are not filled by interpolation in the L2 version as those trajectories are then considered as distinct segments.

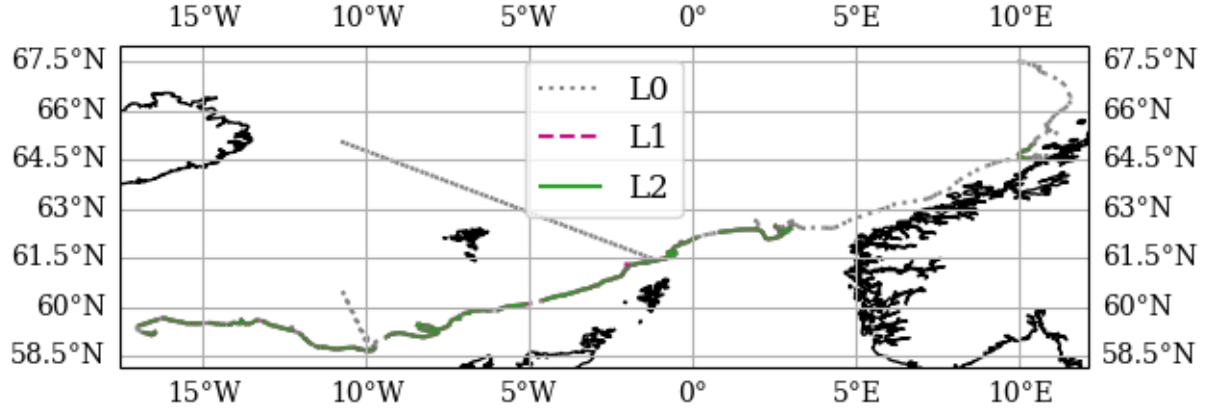


Figure 7: SPOT drifter 0-4498291 data (2025-05-12 – 2025-09-16) at different pre-processing levels.

Figure 8 presents the L2 trajectories of both SPOT and MELODI drifters deployed between Tromsø and Nice during OTC25.

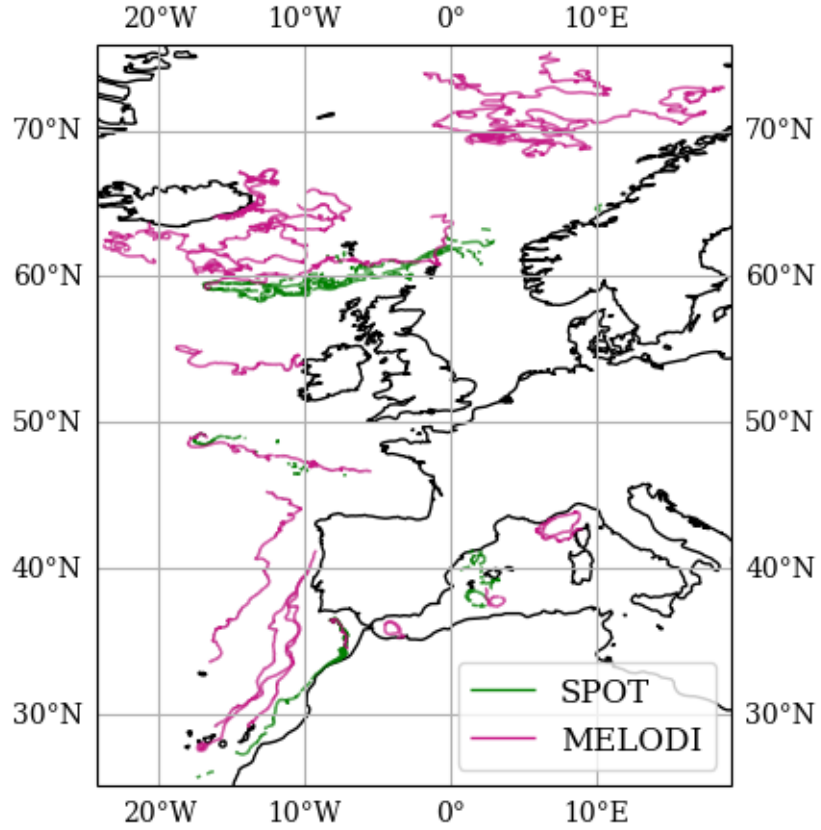


Figure 8: L2 drifters data from the OTC 25 (2025-04-25 – 2025-09-16).

### 2.3 Modeling of drifter trajectories

This section describes the methods used to analyze the drifter trajectories and reconstruct their positions. We first introduce the trajectory reconstruction methods implemented in our analysis and we detail the

metrics employed to evaluate them. Next, we present the Lagrangian statistics used to characterize the drift dynamics.

### 2.3.1 Linear combination

First, the drift is modeled as a simple linear combination of geophysical forcings acting on the object:

$$\frac{d\mathbf{X}(t)}{dt} = (\mathbf{u}_{cg} + \mathbf{u}_e + \mathbf{u}_s + \beta_w \mathbf{u}_w)(t, \mathbf{X}(t)) \quad (1)$$

where  $\mathbf{X}(t)$  is the position of the particle at time  $t$ ,  $\mathbf{u}_{cg}$  is the current velocity vector field estimated from *balanced* SSH,  $\mathbf{u}_e$  is the wind-induced Ekman current velocity vector field,  $\mathbf{u}_s$  is the wave-induced Stokes drift velocity vector field,  $\mathbf{u}_w$  is the wind velocity vector field at the sea surface, weighted by  $\beta_w$ . The notation  $(\cdot)(t, \mathbf{X}(t))$  indicates that the linear combination of the velocity vector fields is interpolated in space and time at the particle position.

The geostrophic approximation is the method classically employed in operational products to derive sea surface currents from SSH by solving the equilibrium between the Coriolis (pseudo-)force and the pressure gradient:

$$f\mathbf{k} \times \mathbf{u}_g = -g\nabla\eta \quad (2)$$

where  $f$  is the Coriolis parameter,  $\mathbf{k}$  is the vertical unit vector,  $\mathbf{u}_g$  the geostrophic velocity vector,  $g$  is the gravitational acceleration and  $\eta$  is the SSH. The geostrophic balance neglects, in particular, the centrifugal acceleration of the flow. This advective term can become significant in intense mesoscale eddies, rings and meanders ([Penven et al., 2014](#)) or in submesoscale structures ([Archer et al., 2025; Tranchant et al., 2025](#)). Accounting for the advection of momentum leads to the cyclogeostrophic equilibrium:

$$\mathbf{u}_{cg} - \frac{\mathbf{k}}{f} \wedge (\mathbf{u}_{cg} \cdot \nabla) \mathbf{u}_{cg} = \mathbf{u}_g \quad (3)$$

where  $\mathbf{u}_{cg}$  is the cyclogeostrophic velocity vector. Solving the cyclogeostrophic equation cannot be done analytically in the general case ([Penven et al., 2014](#)); therefore the VarDyn product uses the cyclogeostrophic inversion method proposed by Bertrand, Le Sommer, et al. ([2025](#)) and implemented in the Python package `jaxparrow` ([Bertrand, Vianna Zaia De Almeida, et al., 2025](#)).

Following classical Ekman theory ([Ekman, 1905](#)), we estimate the Ekman currents at the sea surface as a function of the wind stress at the sea surface provided by ECMWF:

$$\mathbf{u}_e = \frac{1}{\rho\sqrt{2A_z|f|}} \tau e^{i\theta_e} \quad (4)$$

where  $\theta_e = 45^\circ$  controls the deflection of the wind stress vector  $\tau$  (should be multiplied by -1 in the North Hemisphere),  $\rho$  is the seawater density, and  $A_z$  is the vertical eddy viscosity.

The Stokes drift and the wind velocity at the sea surface are directly taken from the observation products as detailed in Section [2.2.1](#).

#### 2.3.1.1 Parameters estimation

Our linear combination model has two free parameters that we propose to tune from the drifters data. The vertical eddy viscosity  $A_z$  is linked to the Ekman depth and varies depending on the mixing conditions in the upper ocean. It is expected to range from  $10^{-2} \text{ m}^2\text{s}^{-1}$  to  $10^{-1} \text{ m}^2\text{s}^{-1}$  in the open ocean under moderate mixing. As the geometry of the drifter does not enter into consideration here, we calibrated this parameter for all the drifters at the same time. We use the tuning parameter  $\beta_w$  to account for the direct effect of the wind on the drifters motion. Since the response of the drifters to the wind may vary due to their specific designs, we calibrated it separately for the MELODI and SPOT drifters, leading to two distinct parameters  $\beta_{w_S}$  for the SPOT design and  $\beta_{w_M}$  for the MELODI design.

The drift function of a drifter can therefore be re-written as:

$$\mathbf{v}_d(t, \mathbf{X}(t); A_z, \beta_{w_S}, \beta_{w_M}) = [\mathbf{u}_{cg} + \mathbf{u}_e + \mathbf{u}_s + (\mathbf{1}_S \beta_{w_S} + \mathbf{1}_M \beta_{w_M}) \mathbf{u}_w](t, \mathbf{X}(t)) \quad (5)$$

where  $\mathbf{1}_S = 1$  (resp.  $\mathbf{1}_M = 1$ ) if the drifter is a SPOT (resp. MELODI) and 0 otherwise.

$\hat{A}_z, \hat{\beta}_{w_S}, \hat{\beta}_{w_M}$  are estimated by solving a non-negative-least-square problem between two consecutive drifter observations, provided that the observations are sufficiently close in time:

$$\hat{A}_z, \hat{\beta}_{w_S}, \hat{\beta}_{w_M} = \arg \min_{A_z, \beta_{w_S}, \beta_{w_M} \geq 0} \sum_i D(\mathbf{X}_{t_i} + \Delta t_i \mathbf{v}_d(t_i, \mathbf{X}_{t_i}; \beta_w), \mathbf{X}_{t_{i+1}})^2 \quad (6)$$

where  $\mathbf{X}_{t_i}$  is an observed drifter position at time  $t_i$  and  $\Delta t_i = t_{i+1} - t_i$  is the time interval between observations  $\mathbf{X}_{t_i}$  and  $\mathbf{X}_{t_{i+1}}$ .

### 2.3.2 Maxey-Riley framework

The Maxey-Riley equations provide an accurate description of floating object drift, making them a useful model for predicting the trajectories of floaters in ocean environments. This framework takes into account all the forces that contribute to their horizontal movement: the *flow force* exerted on the particle by the fluid, the *added mass force* resulting from the displacement of part of the fluid with the particle, the *lift force*, which occurs when the particle rotates while moving in a (horizontal) shear flow, and the *drag force* due to the viscosity of the fluid. Here we present briefly the theory that leads to the Maxey-Riley framework, following Beron-Vera et al. (2019). It is important to keep in mind that, despite its mathematical complexity, it is simply the result of applying Newton's second law:

$$m_p \ddot{x}_p = F_{\text{flow}} + F_{\text{mass}} + F_{\text{lift}} + F_{\text{drag}} \quad (7)$$

where  $m_p$  is the particle mass and  $\ddot{x}_p$  its acceleration.

Let us consider a spherical particle of radius  $a$  and density  $\rho$  floating in the interface between air and water. The *flow force* is given by

$$F_{\text{flow}} = \frac{m_f}{m_p} \frac{Dv_f}{Dt}, \quad (8)$$

where  $m_f$  is the mass of the displaced fluid,  $v_f$  is the fluid velocity and  $\frac{Dv_f}{Dt} = \frac{\partial v_f}{\partial t} + (\nabla v_f)v_f$  stands for material derivative.

The *added mass force* can be expressed as

$$F_{\text{mass}} = \frac{\frac{1}{2}m_f}{m_p} \left( \frac{Dv_f}{Dt} - \dot{v}_p \right), \quad (9)$$

where  $\dot{v}_p = \frac{\partial v_p}{\partial t}$  is the particle acceleration.

The *lift force*, generated by the particle rotation, reads:

$$F_{\text{lift}} = \frac{\frac{1}{2}m_f}{m_p} \omega_f (v_f - v_p)^\perp, \quad (10)$$

where  $\omega_f$  is the vertical vorticity of the fluid and the operator  $^\perp$  indicates a 90° counterclockwise rotation.

Finally, the *drag force* is given by

$$F_{\text{drag}} = \frac{12\mu_f A_f / l_f}{m_p} (v_f - v_p), \quad (11)$$

where  $\mu_f$  is the dynamic fluid viscosity,  $A_f = \pi a^2$  is the projected area of the particle and  $l_a = 2a$  is its projected length.

In order to adapt this fluid mechanics formulation to geophysical flows, a contribution from the Coriolis force is included in the flow and added mass force. The forces are averaged in the vertical direction over the particle's height, with the integration limits being from  $-h$  (immersed depth) to  $h_a$  (height above the surface), since the fluid variables take different values in the water region  $[-h, 0]$  and in the air region  $(0, h_a]$ . This process gives the explicit form of the Maxey-Riley framework:

$$\dot{v}_p + \left( f + \frac{1}{2} Ra \right) v_p^\perp + \tau^{-1} v_p = R \frac{Dv}{Dt} + R \left( f + \frac{1}{2} \omega \right) v^\perp + \tau^{-1} u, \quad (12)$$

where  $f$  is the Coriolis parameter,  $R$  is a parameter that depends on the depth  $h$  of the submerged spherical cap,  $\omega$  is the water vorticity, and  $\tau$  accounts for the inertial response time of the medium to the particle.  $u$  is defined as

$$u = (1 - \alpha)v + \alpha v_a \quad (13)$$

where  $v$  is the water velocity,  $v_a$  the air velocity and  $\alpha$  can be interpreted as a leeway factor. It should be noted that, contrarily to leeway models, where the wind parameter is chosen *ad hoc*, here  $\alpha$  is obtained from geometrical characteristics of the particle and it is not a fit parameter.

The drifters we deployed during the OTC25 campaign were not spheric. This difference is taken into account by a correction factor  $0 \leq \kappa \leq 1$  that changes the value of  $\tau$  and is defined as

$$\kappa^{-1} = \frac{1}{3} \frac{a_n}{a_v} + \frac{2}{3} \frac{a_s}{a_v}, \quad (14)$$

where  $a_n$ ,  $a_s$  and  $a_v$  are the radii of a sphere of the equivalent projected area, surface area and equivalent volume. For the case of a cylinder (like the MELODI drifter), they can be obtained as

$$a_n = \sqrt{\frac{2R_D H_D}{\pi}}, \quad a_s = R_D, \quad \text{and} \quad a_v = \sqrt[3]{\frac{3}{4} R_D^2 H_D}, \quad (15)$$

where  $R_D$  and  $H_D$  are the radius and the height of the cylindric drifter.

It has been shown that rotational effects from Earth are generally negligible when the floating object's dimensions are significantly smaller than approximately 1 km (Wagner et al., 2022). We can thus neglect the Coriolis effect in our measurements, since our drifters are smaller than 30 cm.

We can do one last approximation under the assumption that the particle is small compared to the characteristic lengths of the flow (known as *slow manifold approximation*). In this case, the inertial response time is short and the Maxey-Riley framework can be simplified to:

$$\dot{x}_p = u + \tau u_\tau, \quad \text{with} \quad u_\tau = R + \frac{1}{3} R \omega v^\perp - \frac{Du}{Dt} - \frac{1}{3} R \omega u^\perp \quad (16)$$

where  $u$  is given by Equation 13. This framework is a two-dimensional system in  $x$  and does not require specification of the initial velocity for resolution. This is the equation we used to model the trajectory of the drifters deployed during the campaign.

### 2.3.3 Model evaluation

To evaluate the performance of the trajectory reconstruction methods, we integrate the models over N days using the drifter positions as initial conditions. We then compare the reconstructed trajectories with the observed drifter trajectories using the following metrics:

- **Separation distance:** the separation distance is the distance  $D(\mathbf{X}_{t_i}, \mathbf{Y}_{t_i})$  between the reconstructed final position  $\mathbf{X}_T$  and the drifter's final position  $\mathbf{Y}_T$ . We used the Haversine formula to compute the great-circle distance between two positions, assuming the Earth is a perfect sphere.
- **Liu Index:** the Liu index (Liu & Weisberg, 2011)  $s(\mathbf{X}, \mathbf{Y})$  allows comparison of reconstructions across different regimes by normalizing the cumulative separation distance by the cumulative distance effectively traveled by the reference drifter. It yields a non-dimensional index, where a value of 0 indicates a perfect match between the reconstructed and observed trajectories, and a value of 1 indicates that the reconstruction diverges from the reference as rapidly as the reference itself moves. It is defined as:

$$s(\mathbf{X}, \mathbf{Y}) = \frac{\sum_{t_i=1}^T D(\mathbf{X}_{t_i}, \mathbf{Y}_{t_i})}{\sum_{t_i=1}^T \sum_{t_j=1}^{t_i} D(\mathbf{Y}_{t_{j-1}}, \mathbf{Y}_{t_j})} \quad (17)$$

## 2.4 Pair dispersion

Spreading of a group of surface drifters can be characterized by the distance  $D$  between a pair of drifters and the relative diffusivity  $K$ , defined as:

$$K(D) = \frac{1}{2} \frac{\partial D^2}{\partial t}, \quad (18)$$

where  $t$  stands for the time (Van Sebille et al., 2015). Since we study the motion of floaters at the sea surface, we will use the 2-D Quasi-Geostrophic turbulence theory. In this context, the dynamics of the pair separation can be classified in three regimes, depending on the scale of the underlying currents. There are two important length scales: the Rossby deformation radius, that is the distance at which rotational effects become important, and the scale of the eddies present in the flow.

For separations smaller than the Rossby deformation radius, we expect the pair dispersion  $D^2$  to increase exponentially with time and the pair diffusivity to be proportional to  $D^2$ . This is known as the “exponential regime”. If the separation is bigger than the Rossby deformation radius but smaller than the biggest eddies in the flow, the dynamics is known as “Richardson regime” and is expected to scale as  $D^2 \propto t^3$ . The pair diffusivity is expected to be  $K \propto D^{4/3}$ . These two regimes are *local*, meaning that their dynamics is governed by eddies of  $\mathcal{O}(D)$ . For scales larger than the eddies, i.e., for non-local dynamics, we expect a diffusive random walk regime with dispersion scaling linearly with time and  $K$  keeping a constant value. In this case, the diffusive character of the dynamics arises because each drifter of the pair is influenced by different, uncorrelated eddies.

We performed four deployments of five SPOT drifters each dedicated to study pair dispersion, as shown in Figure 3. The first deployment was performed on the 12th May on the Atlantic Sea, the second on the 18th May, the third on the 24th May just before crossing Gibraltar Strait, and one last deployment on May 30th at the mediterranean sea.

Source: [Instruments, data and methods](#)

## 3 Results

In this section, we present the trajectory reconstruction performances of the drift models presented in Section 2.3, and the dispersion characteristics of the drifters ensembles in the different regions of deployment.

### 3.1 Modeling of drifter trajectories

Two models were used to reconstruct the drifter trajectories: a linear combination model (Section 2.3.1) and the Maxey-Riley framework (Section 2.3.2).

#### 3.1.1 Linear combination

Before employing the linear combination model, we first estimated the parameters controlling the Ekman current magnitude (i.e.  $A_z$ ) and the windage coefficients (i.e.  $\beta_{w_S}$  and  $\beta_{w_M}$ ) from the SPOT and MELODI drifter observations, as described in Section 2.3.1.1.

As can be seen in Table 2, the vertical eddy viscosity  $A_z$  estimated from the drifter data is  $0.027 \text{ m}^2\text{s}^{-1}$ , which is within the expected range for open ocean conditions. However, the windage coefficients are lower than expected, with values of 0.092 % and 0.65 % for the SPOT and MELODI drifters respectively, while expected values are usually between 1 % to 3 %.

Table 2: Estimated parameters of the linear combination model (Equation 5) after performing a non-negative-least-squares fit on the L1 processed drifter data.

$A_z(\text{m}^2\text{s}^{-1})$	$\beta_{w_S}(\%)$	$\beta_{w_M}(\%)$
0.027	0.092	0.65

Using the estimated parameters, we then reconstructed 7-days drifter trajectories as solutions to the ODE given by Equation 1. To keep this report short, we decided to focus on the MELODI drifters as they provide higher-frequency GPS data compared to the SPOT drifters. We selected three MELODI drifters released in different locations and under varying oceanic and atmospheric conditions:

- #301434060093370 deployed in the Lofoten Vortex on April 25, 2025, characterized by strong balanced currents and winds,
- #301434060982270 deployed off the coast of Portugal on May 24, 2025, under weak balanced currents and moderate winds,
- #301434060983290 deployed in the Balearic Sea on June 1, 2025, in a strong cyclonic structure and almost no wind except for a brief blow from the East.

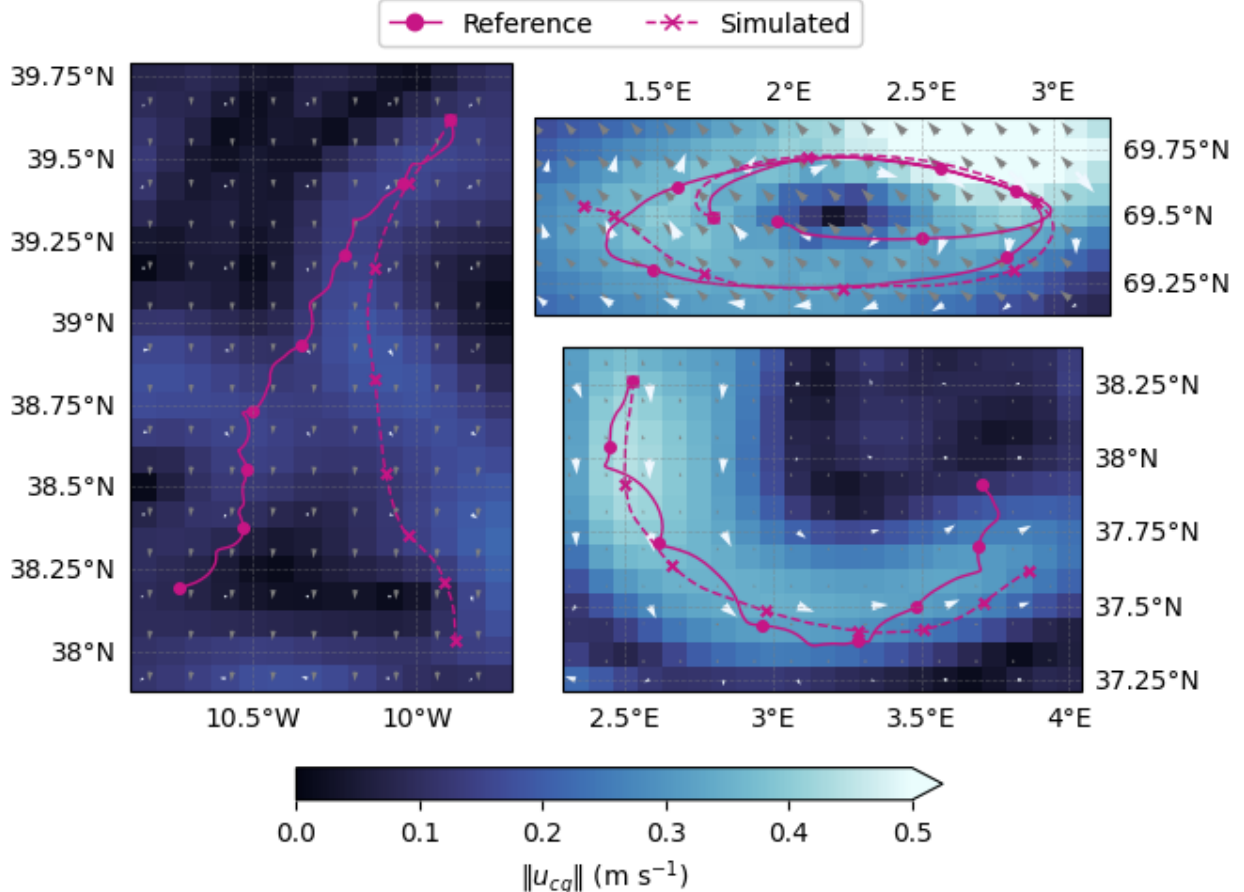


Figure 9: Linear combination model (Equation 5) estimated trajectories over a 7-day horizon (dashed lines) against the true drifter trajectories (solid lines) for three different MELODI drifters deployed in the Lofoten Vortex (top right), off the Portuguese Coast (left), and in the Balearic Sea (bottom right). Markers indicate daily positions along the trajectories. Background colors indicate the magnitude of the cyclogeostrophic current from the VarDyn and white arrows give their velocity, while grey arrows represent wind velocity from the ERA5 reanalysis.

The reconstructed trajectories (dashed lines) are shown in Figure 9 against the true drifter trajectories (solid lines) over a 7-day horizon. Markers indicate daily positions along the trajectories. Background colors indicate the magnitude of the cyclogeostrophic current from the VarDyn and white arrows give their velocity, while grey arrows represent wind velocity from the ERA5 reanalysis. The geophysical fields are represented at for the center timestamp of each trajectory. Metrics quantifying the reconstruction performance, namely the final separation distance and the Liu index, are reported in Table 3.

It can be seen that the reconstructed trajectory in the Lofoten Vortex (top right panel of Figure 9) closely follows the true drifter trajectory but at a much slower pace. It suggests that the cyclogeostrophic currents are well captured by the VarDyn product, but that the Ekman current (usually the second largest term in a linear combination drift model) might be underestimated. Because of the strong winds and currents, another possible explanation for this discrepancy could be an inaccurate representation of the wind-current interactions. This results in a final separation distance of approximately 29 km after 7 days, and a Liu Index of 0.23, indicating that the estimation separates four times more slowly than the drifter moves.

The trajectory reconstructed off the Portuguese coast (left panel of Figure 9) shows a larger deviation from the true drifter trajectory, with a final separation distance of approximately 76 km and a Liu index of 0.32. By

looking at Figure 9, it appears that the drifter followed a small-scale structure heading South-South-East and not captured by satellite-derived observations products, while the reconstruction follows a current oriented slightly more to the West.

Finally, the trajectory reconstructed in the Balearic Sea (bottom right panel of Figure 9) shows an overall very good agreement with the true drifter trajectory, with a final separation distance of approximately 35 km but more importantly a Liu index of 0.1, meaning that the distance between the estimation and the reference grows ten times slowly than the drifter displaces. The westward gust of wind is clearly visible in the reference trajectory because of the inertial oscillations it generates, a process that is not represented at all in the linear combination drift model.

Table 3: Performances of the linear combination model (Equation 5) in three distinct regions and conditions.

Region	Separation distance (km)	Liu Index
Lofoten Vortex	29	0.23
Portuguese Coast	76	0.32
Balearic Sea	35	0.10

### 3.1.2 Maxey-Riley framework

We will use the data from MELODI drifters since they provide a better time resolution than the SPOT drifters (they transmit in regular intervals). As shown in Figure 2, they are not spherical. To take their shape into account, we calculate the radius of the sphere with equivalent projected area, surface area and equivalent volume (Equation 15), obtaining  $a_n = 0.08$  m,  $a_s = 0.12$  m and  $a_v = 0.11$  m. The weight on the bottom of the drifters is not taken into account for this calculations but the total weight of the drifter is considered to calculate its density. We use a combination of all the currents present at the surface to compute  $v_f$  (Ekman, Stokes and the cyclogesotrophic currents) and the wind at the surface to compute  $v_a$ .

We consider three representative cases: a deployment in the Norwegian Sea, one in the Atlantic Ocean and one in the Mediterranean Sea. Figure 10 shows the drifter real trajectory for a week after release in the Lofoten Vortex on the 24th April and the reconstructed trajectory from the Maxey-Riley framework, obtained using Equation 16. We can observe that the reconstructed trajectory follows the general tendency of the real one but it does not exactly follow the same path, and seems to move with a slower speed than the real drifter. It is worth noting that the drifter seems to be highly influenced by the wind (blowing northward).

Figure 11 shows the real and simulated trajectories for a deployment made in the Atlantic Ocean on the 23rd May. Remarkably, in this case the simulated trajectory is really close to the real one. Nevertheless, it does not seem to take into account the small scale oscillations visible in the real trajectory. These oscillations are usually generated by waves and are not visible in the sattelite data, which could explain why the simulation did not account for them.

It is important to remind that these numerical resolutions do not have any fitting parameter. They only depend on the currents and wind fields (products derived from sattelite data), the initial position of the drifter and its geometry. The numerical resolution is thus very sensitive to changes in those parameters. For example, several runs of the simulation with slight changes of the initial position give rise to a different outcome, which may not be close to the real one. Figure 12 shows the real and simulated trajectories for a deployment made in the Mediterranean Sea on the 30th May. In this case, the deployment was made at the interface between two vortices and the wind was blowing westward. The simulated trajectory does not follow the real one. We will discuss the possible reasons in the Section 4.

## 3.2 Pair dispersion

We used the home-made SPOT drifters to study pair dispersion. They are designed to transmit their position every 30 minutes. However, this is not always the case. In order to calculate the distance between a pair of drifters, they should have transmitted in the same time interval. Figure 13 shows in black when each drifter transmitted its position, using a time interval of 30 minutes. This trajectories have already been interpolated

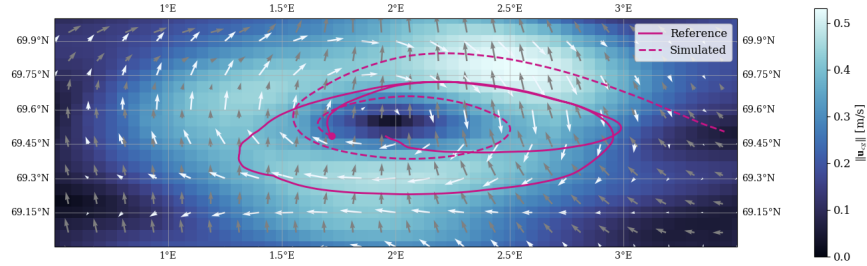


Figure 10: Drifter trajectory on the Lofoten Vortex during one week after deployment. The solid lines indicate the real trajectory, while the dashed lines show the result of solving the Maxey-Riley set. The colors indicate the absolute value of the cyclogeostrophic current at the moment of release. The white arrows show the direction of the current and the gray arrows indicate the wind direction.

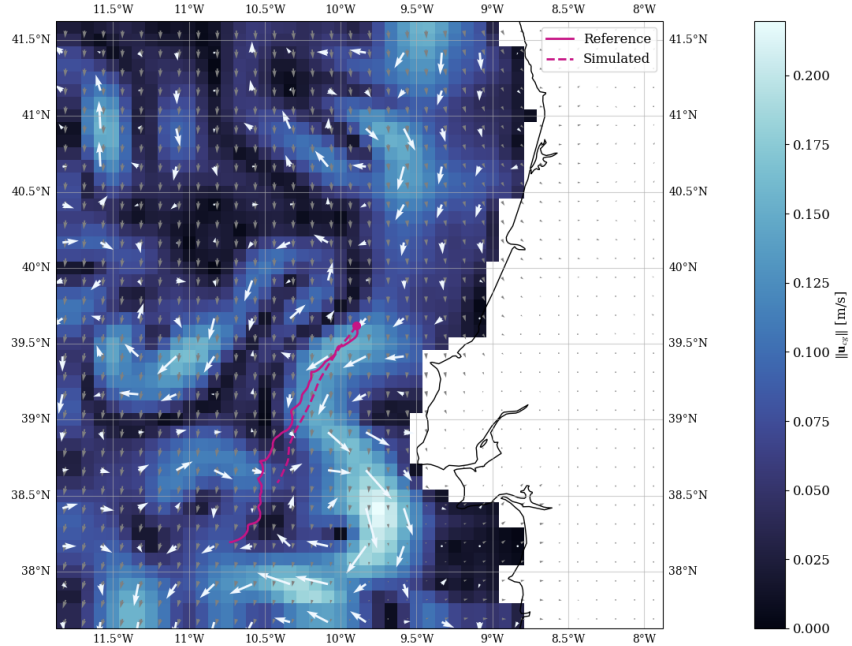


Figure 11: Drifter trajectory in the Atlantic Ocean, near the Portuguese coast, during one week after deployment. The solid lines indicate the real trajectory, while the dashed lines show the result of solving the Maxey-Riley set. The colors indicate the absolute value of the cyclogeostrophic current at the moment of release. The white arrows show the direction of the current and the gray arrows indicate the wind direction.

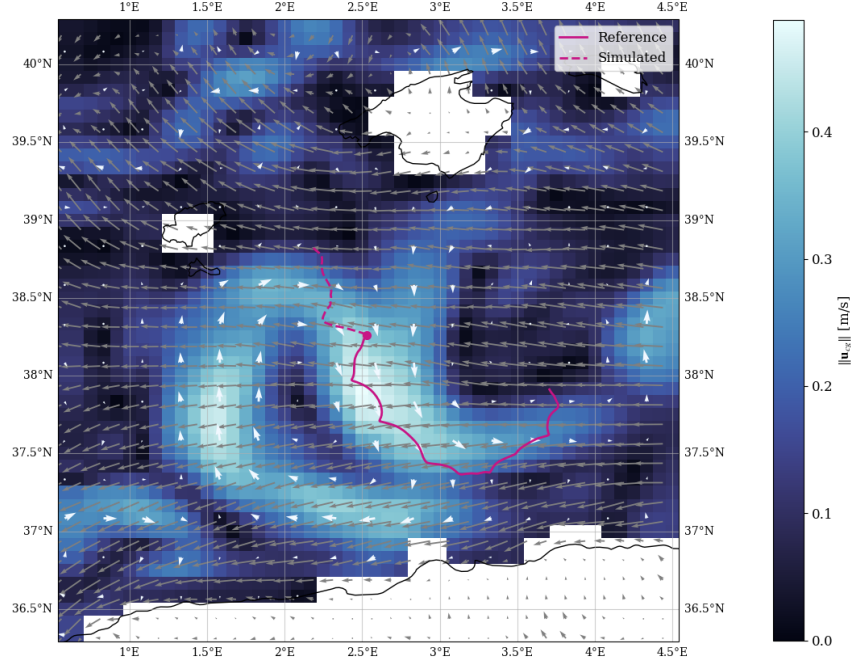


Figure 12: Drifter trajectory on the Mediterranean Sea during one week after deployment. The solid lines indicate the real trajectory, while the dashed lines show the result of solving the Maxey-Riley set. The colors indicate the absolute value of the cyclogeostrophic current at the moment of release. The white arrows show the direction of the current and the gray arrows indicate the wind direction.

in time (L2 version). For each deployment of  $N = 5$  drifters, there are  $N(N - 1)/2 = 10$  pairs. For each pair, we will consider their positions if they transmitted at the same time interval.

Considering the variability of the conditions for making *in-situ* measurements, each group of drifters behave differently. We can observe that there are several pairs for the first and third deployments, but less simultaneous transmissions for the second and fourth. For example, on the last deployment one drifter stop transmitting almost immediately, so we have only 6 pairs. But if we take a closer look at Figure 13 (d) we see that in practice we have only one pair of drifters that transmitted for more than a month.

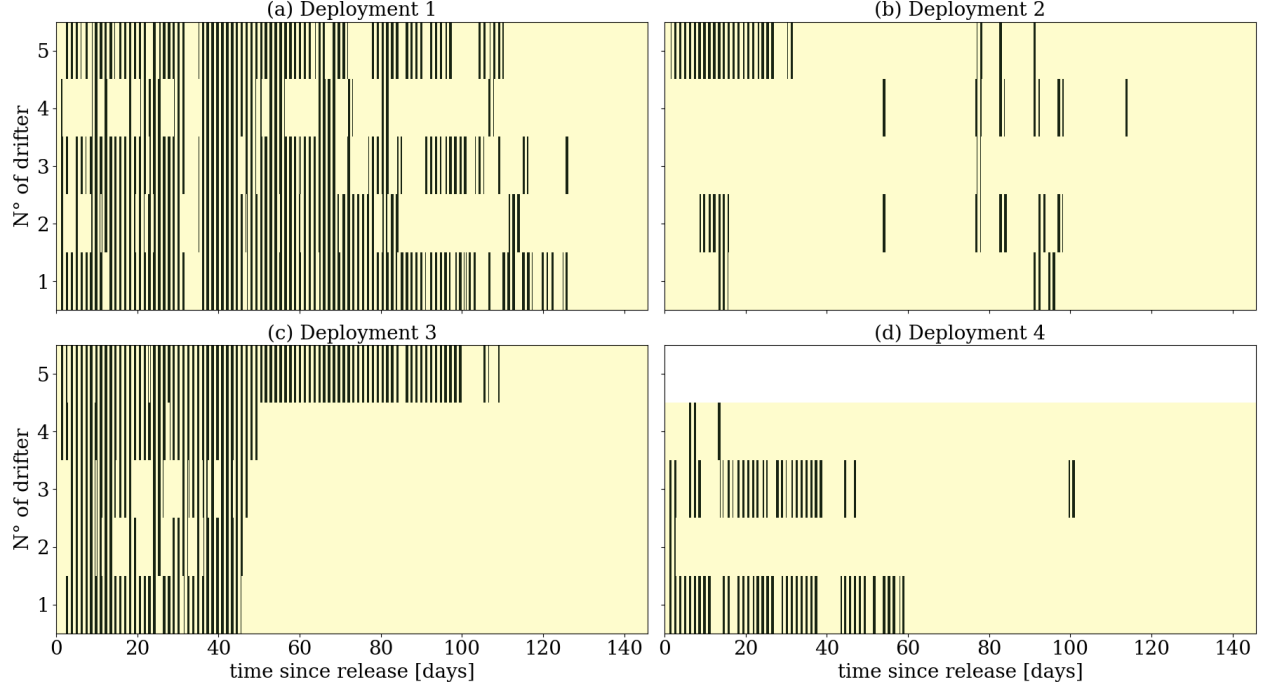


Figure 13: Mask showing if the drifters transmitted their position. The black rectangles indicate that the transmission was successful, yellow rectangles indicate that they did not transmit. L2 trajectories are used for the analysis.

Figure 14 shows the pair dispersion  $D^2$  as a function of time for each deployment. As discussed before, for the first and third deployments we have several pairs while we do not have enough data for the second and fourth. In Figure 14 (a) we can clearly observe two different behaviors: an exponential growth for the first two weeks after release, and a different regime after. Pink lines indicate the exponential and the Richardson regimes, showing a good agreement with the measured data. The third deployment, however, seems to show only an exponential behavior. It follows a scaling law  $D^2 \propto e^{\alpha t}$ , with a growth rate of  $\alpha = 5$ . Unexpectedly, this growth rate is bigger than the one of the first deployment but the particles remain in an exponential regime. This can be due to a difference in transition thresholds. If the transition scale (the size of the biggest eddies in the flow) varies, we expect the first group of drifters to reach the Richardson regime sooner despite slower growth, while the third group of drifters remain in exponential regime but still relatively close together, not yet having reached their larger transition threshold.

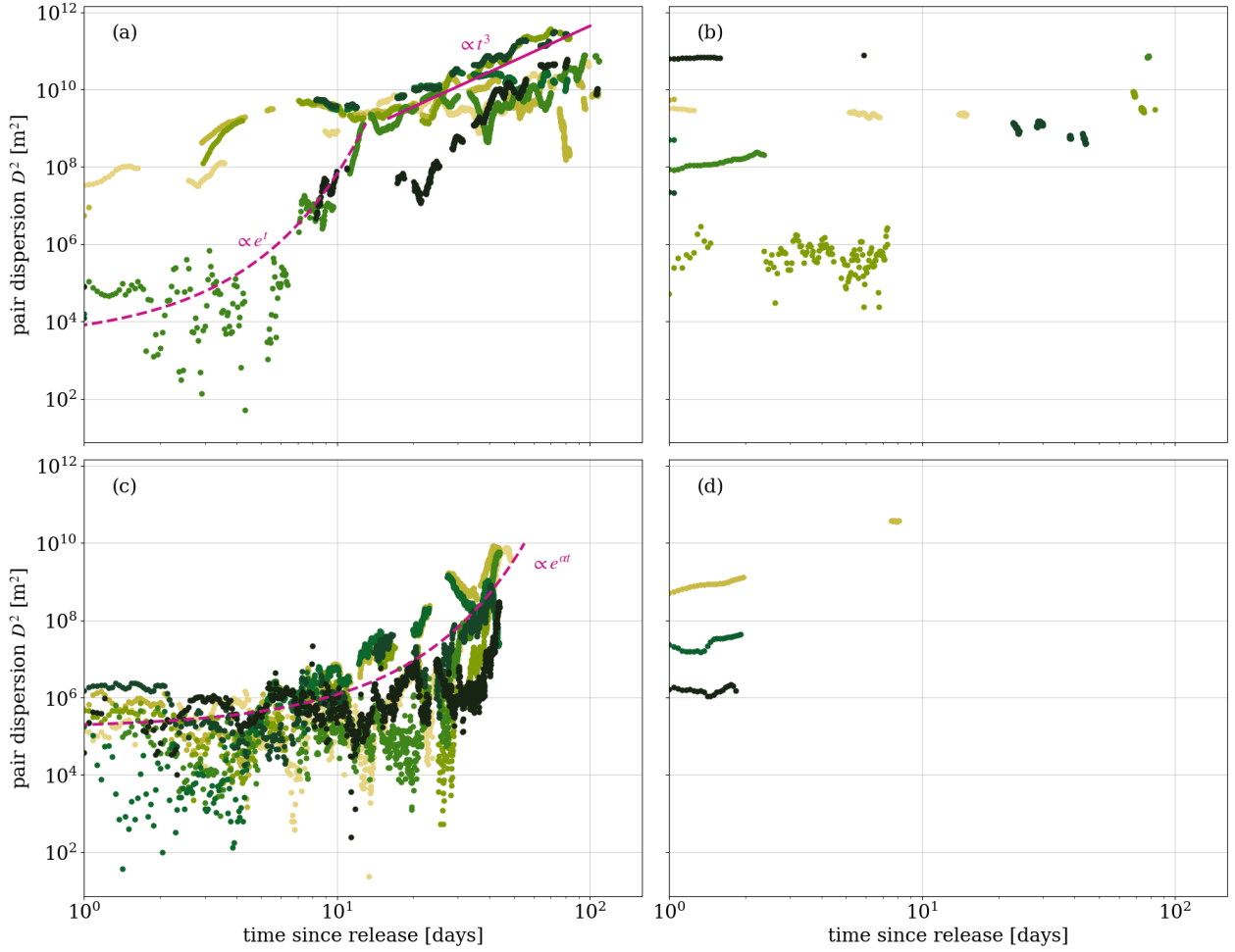


Figure 14: Pair dispersion for each deployment as a function of the time since release. The colors represent the different pairs. The pink dashed line shows the scaling corresponding to the exponential regime and the solid pink line represents the scaling of the richardson regime.

The rate of change of separation, or pair diffusivity, has been calculated using Equation 18 and is shown in Figure 15. Both regimes are shown for all deployments. For the first one, it does not seem to be so clear that there are two regimes, as it was in Figure 14 (a). The third one, however, shows one clear tendency where  $K \propto D^2$ . The second and fourth deployment do not have enough data to determine the regime that governs its dynamics.

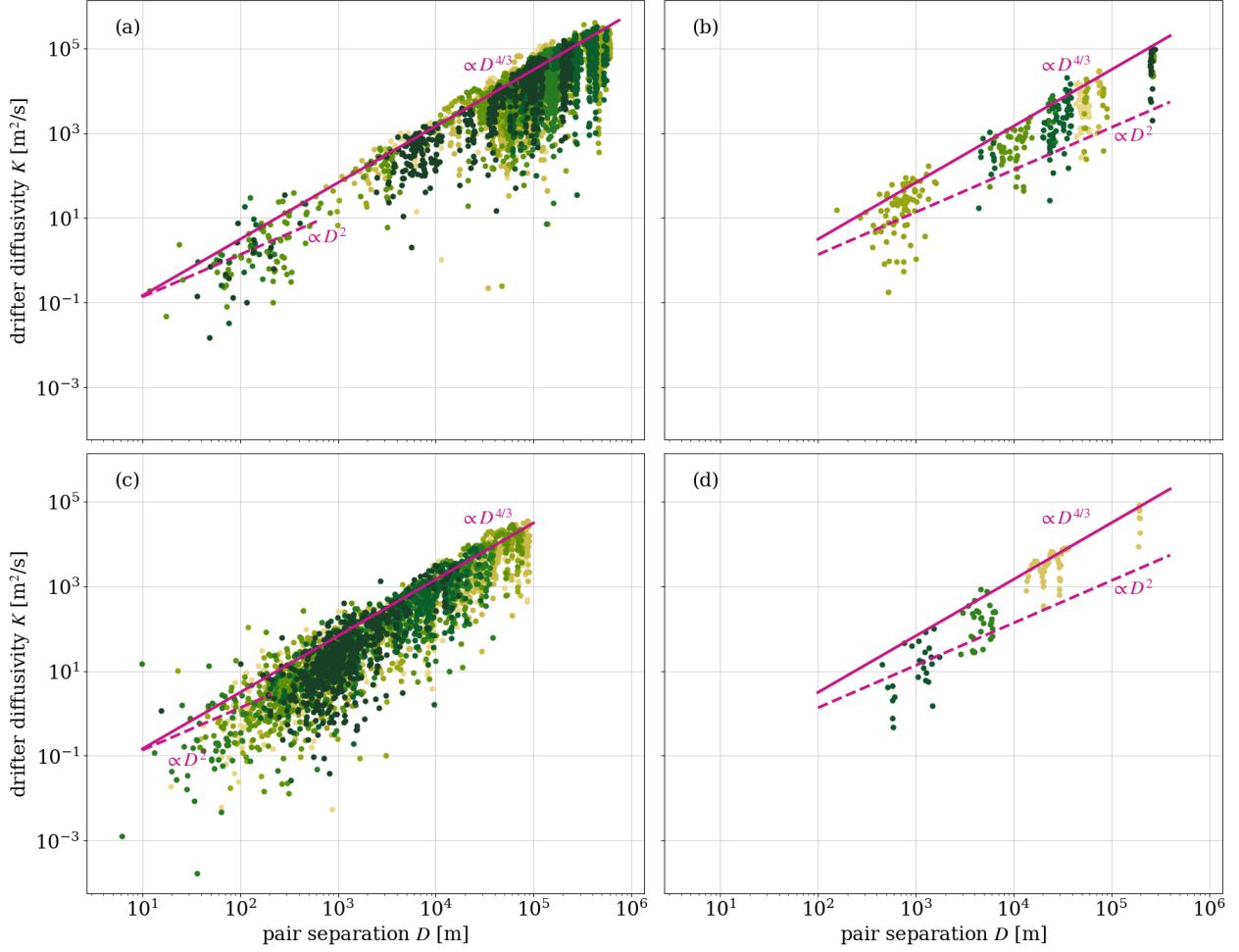


Figure 15: Pair diffusivity as a function of the distance between pairs. The colors represent the different pairs. The pink dashed line shows the scaling corresponding to the exponential regime and the solid pink line represents the scaling of the richardson regime.

Source: [Results](#)

## 4 Discussion

### 4.1 Modeling of drifter trajectories

#### 4.1.1 Linear combination

By nature the linear combination model has a limited expressive power as it assumes that the drifter velocity is a weighted sum of only four components: the cylogeostrophic current, the Ekman current, the Stokes drift, and the leeway. We choose to parameterize and calibrate some of this terms but from the drifter GPS data, but assessing their estimated values is not trivial. Some of the drifter deployments during the campaign were filmed using drones, which could be used to validate or better estimate some estimated parameters, especially the windage coefficients. Additional terms could also be added to the model in order to account for other processes affecting the drifter motion, such as inertial oscillations ([Sykulski et al., 2016](#)) or tidal currents.

Drifter trajectories are not only affected by large-scale features, but also by small-scale eddies, fronts, or filaments, which are not yet resolved by satellite-derived current products. One way to account for these small-scale structures is to use stochastic representations of the drift and reconstruct ensembles of probable

trajectories (Brolly, 2023; Mínguez et al., 2012; Sykulski et al., 2016). However, it is not clear how to calibrate such stochastic models, especially as the unresolved small-scale features are not homogeneous in space and time. Recent developments in machine learning could be leverage to learn a map from satellite observations capturing small-scale structures (such as sea surface temperature, ocean color, or surface roughness) to physical parameters (including in a stochastic setting) from drifter observations (Cheng et al., 2023; Thorey et al., 2017).

We presented here only three drifter trajectory reconstructions, but a more comprehensive evaluation of the model performance could be conducted using all drifters deployed during the campaign, including the OMB and CLS drifters.

#### 4.1.2 Maxey-Riley framework

Surprisingly, the Maxey-Riley framework has been used only once to describe the dynamics of floating particles in the ocean (Olascoaga et al., 2020). Yet it is the theory derived from first principles that accounts for the forces exerted on a floating particle at the interface between a fluid and air. Unlike most theories that describe particle motion in the ocean, this model does not have fitting parameters. One typical fitting parameter in studies on search and rescue (Breivik & Allen, 2008) is the leeway coefficient, that accounts for windage effects. In the framework of Equation 16, the parameters  $\alpha$ ,  $R$  and  $\tau$  are calculated based on the particle geometry and the properties of the objects and the fields (density, viscosity).

Passing from the full Maxey-Riley equations (Equation 12) to the slow manifold approximation (Equation 16) facilitates numerical resolution since we passed from a second order differential equation (that is, two ordinary differential equations with two initial conditions) to a first order differential equation. We only need the initial position of the drifter but not its initial velocity. Taking a look at Figure 12 we could think that the slow manifold approximation may have been an overstatement. However, the only assumption there is that the drifter size is smaller than the characteristic lengths present in the system, which remains true. Let us review which assumptions we made may modify significantly the behavior of the numerical simulations.

First, we can wonder if the parameter  $\alpha$ , equivalent to a leeway coefficient, is well determined, since the wind seems to have an important effect on the obtained trajectories. We obtained a value of  $\alpha = 1\%$ , slightly smaller than the typical 3% commonly used as a leeway coefficient. We thus conclude that the mismatch between the trajectories must come from somewhere else.

MELODI drifters are not spheres, but are not perfect cylinders either. The correction  $\kappa$  (Equation 14) that accounts for the deviation from a sphere is not exactly well calculated because it is not straightforward to determine the radii of the equivalent sphere taking into account the metallic anchor included in the MELODI drifters. This discrepancy could be a source of error, because we are not only obtaining  $\kappa$  from these values but also the density of the drifters. When more data from other drifters becomes available, we will compare our results to drifters with different geometries.

Another possible source of error is the spatial and temporal resolution of satellite data. To accurately compute a numerical resolution of Equation 16, we need a short temporal step (for example, one minute). But the satellite data is not available in such short periods and it is thus interpolated. A similar mechanism occurs with the spatial data. Satellites do not retrieve information on the small scales that affect the drifter movement. The Maxey-Riley framework assumes that we know the fields in the scales we need them but this is not the case. We think this is the biggest source of discrepancy between the real trajectories and the simulated ones. Nevertheless, the Maxey-Riley set provides a remarkably accurate description using only the initial position, and we are still working on exploiting its potential to understand the dynamics of floating objects in the ocean.

## 4.2 Pair dispersion

From the data from the first deployment, we could distinguish two different regimes (see Figure 14). However, the separation between them was not clear on the pair diffusivity (Figure 15). The change of regime arrives at approximately two weeks after the deployment, when the distance between pairs is around 70 km. Figure 16 shows the position of the ship, the drifters and the cyclogesotrophic current from the release until this

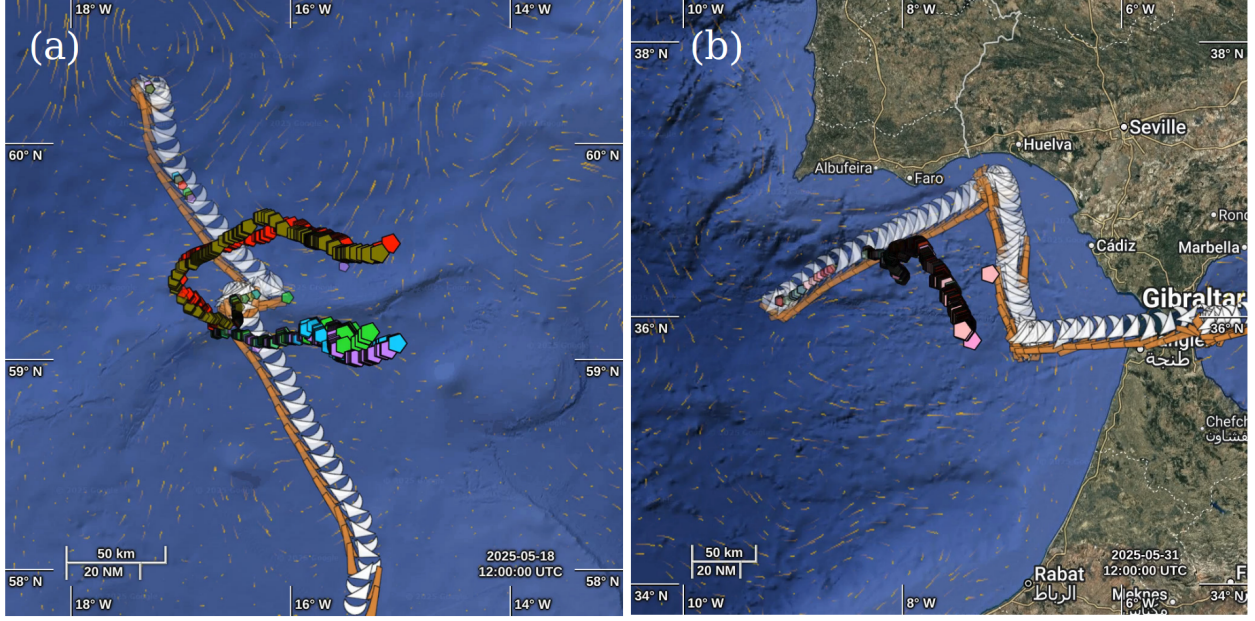


Figure 16: Seashots taken from OVL OceanDataLab, showing the trajectory of the Statsraad Lehmkuhl, the cyclogesotrophic current (from Vardyn) and the position of the SPOT drifters over two weeks, starting the day of the deployment for (a) the first deployment and (b) the third one.

moment. In the panel (a) we can see the seashot corresponding to the first deployment. We can observe that the distance  $D$  is of the order of the eddies, but not yet the biggest eddies present in the flow. It makes sense that, in this case, the dynamics is still local but changes from a regime where they have been in the same eddy to an intermediate one. At the moment of the writing, five months after the release, the system did not reach yet the diffusive regime.

Regarding the third deployment, we can interpret the results shown in the previous section by looking at Figure 16. Two weeks after the deployment, the drifters move still all together and the distance they travelled is much smaller than the eddies present in the flow. It is expected, in this case, that the system remains in a local regime for longer. Our observations are in agreement with the previous results from the literature (Van Sebille et al., 2015) (Röhrs et al., 2023), including the specific two week interval before the transition between regimes in the North Sea (Meyerjürgens et al., 2020).

Source: [Discussion](#)

## 5 Conclusion

During the campaign, we deployed 43 drifters of five different types and successfully modelled their trajectories using two independent approaches. Performances of both methods reveal that drifter motion is governed by (i) small-scale currents that remain poorly resolved in satellite observations, (ii) direct wind forcing, whose impact remain hard to quantify in practice.

Additionally, we analyzed relative pair dispersion for drifter groups of identical type. Our results show an initial exponential growth phase transitioning to Richardson-regime scaling behavior, consistent with established theoretical predictions and previous observational studies. This work is ongoing, and further analysis will be conducted once the remaining drifter trajectories are recovered.

## 6 Acknowledgements



We want to thank ESA for giving us the opportunity to participate in the Ocean Training Course 2025. We thank Craig Donlon, Fabrice Collard and Johnny Johannessen for organizing the campaign. We thank Alexey Mironov for technical help with the drifters. We thank everyone that helped us deploy and follow the drifters. We thank the amazing group of people we had the honour to work and live with.

## References

- Archer, M., Wang, J., Klein, P., Dibarbour, G., & Fu, L.-L. (2025). Wide-swath satellite altimetry unveils global submesoscale ocean dynamics. *Nature*, 640(8059), 691–696. <https://doi.org/10.1038/s41586-025-08722-8>
- Beron-Vera, F., Olascoaga, M., & Miron, P. (2019). Building a maxey–riley framework for surface ocean inertial particle dynamics. *Physics of Fluids*, 31(9).
- Bertrand, V., Le Sommer, J., Vianna Zaia De Almeida, V., Samson, A., & Cosme, E. (2025). A Robust Variational Framework for Cyclogeostrophic Ocean Surface Current Retrieval. *EGUsphere*, 1–22. <https://doi.org/10.5194/egusphere-2025-4172>
- Bertrand, V., Vianna Zaia De Almeida, V., Le Sommer, J., & Cosme, E. (2025). Jaxparrow. Zenodo. <https://doi.org/10.5281/zenodo.14871648>
- Breivik, Ø., & Allen, A. A. (2008). An operational search and rescue model for the norwegian sea and the north sea. *Journal of Marine Systems*, 69(1-2), 99–113.
- Brolly, M. T. (2023). Inferring ocean transport statistics with probabilistic neural networks. *Journal of Advances in Modeling Earth Systems*, 15(6), e2023MS003718. <https://doi.org/10.1029/2023MS003718>
- Calvert, Ross, McAllister, M., Whittaker, C., Raby, A., Borthwick, A., & Van Den Bremer, T. (2021). A mechanism for the increased wave-induced drift of floating marine litter. *Journal of Fluid Mechanics*, 915, A73.
- Calvert, R., Peytavin, A., Pham, Y., Duhamel, A., Zanden, J. van der, Essen, S. van, et al. (2024). A laboratory study of the effects of size, density, and shape on the wave-induced transport of floating marine litter. *Journal of Geophysical Research: Oceans*, 129(7), e2023JC020661.
- Cheng, S., Quilodrán-Casas, C., Ouala, S., Farchi, A., Liu, C., Tandeo, P., et al. (2023). Machine Learning With Data Assimilation and Uncertainty Quantification for Dynamical Systems: A Review. *IEEE/CAA Journal of Automatica Sinica*, 10(6), 1361–1387. <https://doi.org/10.1109/JAS.2023.123537>
- Christensen, K. H., Breivik, Ø., Dagestad, K.-F., Röhrs, J., & Ward, B. (2018). Short-term predictions of oceanic drift. *Oceanography*, 31(3), 59–67.
- Clark, L. K., DiBenedetto, M. H., Ouellette, N. T., & Koseff, J. R. (2020). Settling of inertial nonspherical particles in wavy flow. *Physical Review Fluids*, 5(12), 124301.
- DiBenedetto, M. H., Clark, L. K., & Pujara, N. (2022). Enhanced settling and dispersion of inertial particles in surface waves. *Journal of Fluid Mechanics*, 936, A38.
- Ekman, V. W. (1905). On the influence of the earth rotation on ocean currents. *Arkiv for Matematik, Astronomi Och Fysik*, 2, 1–52.
- Eliot, Shane, Lumpkin, R., Perez, R. C., Lilly, J. M., Early, J. J., & Sykulski, A. M. (2016). A global surface drifter data set at hourly resolution. *Journal of Geophysical Research: Oceans*, 121(5). <https://doi.org/10.1002/2016JC011716>
- Eliot, S., Lumpkin, R., Perez, R. C., Lilly, J., Early, J., & Sykulski, A. (2016). A global surface drifter data set at hourly resolution. *Journal of Geophysical Research: Oceans*, 121(5), 2937–2966.
- GLOBAL\_ANALYSISFORECAST\_WAV\_001\_027. (2023). Global ocean waves analysis and forecast [Data set]. E.U. Copernicus Marine Service Information (CMEMS). Marine Data Store (MDS). <https://doi.org/10.48670/moi-00017>
- Le Guillou, F., Chapron, B., & Rio, M.-H. (2025). VarDyn: Dynamical Joint-Reconstructions of Sea Surface Height and Temperature From Multi-Sensor Satellite Observations. *Journal of Advances in Modeling Earth Systems*, 17(4), e2024MS004689. <https://doi.org/10.1029/2024MS004689>
- Liu, Y., & Weisberg, R. H. (2011). Evaluation of trajectory modeling in different dynamic regions using normalized cumulative Lagrangian separation. *Journal of Geophysical Research*, 116. <https://doi.org/10.1029/2010JC006837>
- Maxey, M. R., & Riley, J. J. (1983). Equation of motion for a small rigid sphere in a nonuniform flow. *The Physics of Fluids*, 26(4), 883–889.
- MELODI. (2024). Retrieved from <https://www.eodyn.com/melodi-2/>
- Meyerjürgens, J., Ricker, M., Schakau, V., Badewien, T. H., & Stanev, E. V. (2020). Relative dispersion of surface drifters in the north sea: The effect of tides on mesoscale diffusivity. *Journal of Geophysical Research: Oceans*, 125(8), e2019JC015925.
- Mínguez, R., Abascal, A. J., Castanedo, S., & Medina, R. (2012). Stochastic Lagrangian trajectory model for drifting objects in the ocean. *Stochastic Environmental Research and Risk Assessment*, 26(8), 1081–1093.

<https://doi.org/10.1007/s00477-011-0548-7>

- Olascoaga, M., Beron-Vera, F., Miron, P., Triñanes, J., Putman, N., & Lumpkin, G. J., R .and Goni. (2020). Observation and quantification of inertial effects on the drift of floating objects at the ocean surface. *Physics of Fluids*, 32(2).
- Penven, P., Halo, I., Pous, S., & Marié, L. (2014). Cyclogeostrophic balance in the Mozambique Channel. *Journal of Geophysical Research: Oceans*, 119(2), 1054–1067. <https://doi.org/10.1002/2013JC009528>
- Quilfen, Y., & Chapron, B. (2019). Ocean surface wave-current signatures from satellite altimeter measurements. *Geophysical Research Letters*, 46(1), 253–261.
- Röhrs, J., Sutherland, G., Jeans, G., Bedington, M., Sperrevik, A. K., Dagestad, K.-F., et al. (2023). Surface currents in operational oceanography: Key applications, mechanisms, and methods. *Journal of Operational Oceanography*, 16(1), 60–88.
- SPOT. (2024). Retrieved from <https://github.com/vadmbertr/otc25-cannelloni>
- Sutherland, B. R., DiBenedetto, M., Kaminski, A., & Van Den Bremer, T. (2023). Fluid dynamics challenges in predicting plastic pollution transport in the ocean: A perspective. *Physical Review Fluids*, 8(7), 070701.
- Sykulski, A. M., Olhede, S. C., Lilly, J. M., & Danioux, E. (2016). Lagrangian Time Series Models for Ocean Surface Drifter Trajectories. *Journal of the Royal Statistical Society Series C: Applied Statistics*, 65(1), 29–50. <https://doi.org/10.1111/rssc.12112>
- Thorey, J., Mallet, V., & Baudin, P. (2017). Online learning with the Continuous Ranked Probability Score for ensemble forecasting. *Quarterly Journal of the Royal Meteorological Society*, 143(702), 521–529. <https://doi.org/10.1002/qj.2940>
- Tranchant, Y.-T., Legresy, B., Foppert, A., Pena-Molino, B., & Phillips, H. (2025). SWOT Reveals Fine-Scale Balanced Motions Driving Near-Surface Currents and Dispersion in the Antarctic Circumpolar Current. *Earth and Space Science*, 12(8). <https://doi.org/10.1029/2025EA004248>
- Van Sebille, E., Waterman, S., Barthel, A., Lumpkin, R., Keating, S. R., Fogwill, C., & Turney, C. (2015). Pairwise surface drifter separation in the western pacific sector of the southern ocean. *Journal of Geophysical Research: Oceans*, 120(10), 6769–6781.
- Van Sebille, E., Aliani, S., Law, K. L., Maximenko, N., Alsina, J. M., Bagaev, A., et al. (2020). The physical oceanography of the transport of floating marine debris. *Environmental Research Letters*, 15(2), 023003.
- Wagner, T. J., Eisenman, I., Ceroli, A. M., & Constantinou, N. C. (2022). How winds and ocean currents influence the drift of floating objects. *Journal of Physical Oceanography*, 52(5), 907–916.
- WIND\_GLO\_PHY\_L4\_NRT\_012\_004. (2024). Global ocean hourly sea surface wind and stress from scatterometer and model [Data set]. E.U. Copernicus Marine Service Information (CMEMS). Marine Data Store (MDS). <https://doi.org/10.48670/moi-00305>